

# Towards a comprehensive model of Earth's disk-integrated Stokes vector

A. García Muñoz

*ESA Fellow, ESA/RSSD, ESTEC, 2201 AZ Noordwijk, the Netherlands*

---

## Abstract

A significant body of work on simulating the remote appearance of Earth-like exoplanets has been done over the last decade. The research is driven by the prospect of characterizing habitable planets beyond the Solar System in the near future. In this work, I present a method to produce the disk-integrated signature of planets that are described in their three-dimensional complexity, *i.e.* with both horizontal and vertical variations in the optical properties of their envelopes. The approach is based on Pre-conditioned Backward Monte Carlo integration of the vector Radiative Transport Equation and yields the full Stokes vector for outgoing reflected radiation. The method is demonstrated through selected examples inspired by published work at wavelengths from the visible to the near infrared and terrestrial prescriptions of both cloud and surface albedo maps. I explore the performance of the method in terms of computational time and accuracy. A clear advantage of this approach is that its computational cost does not appear to be significantly affected by non-uniformities in the planet optical properties. Earth's simulated appearance is strongly dependent on wavelength; both brightness and polarisation undergo diurnal variations arising from changes in the planet cover, but polarisation yields a better insight into variations with phase angle. There is partial cancellation of the polarised signal from the northern and southern hemispheres so that the outgoing polarisation vector lies preferentially either in the plane parallel or perpendicular to the planet scattering plane, also for non-uniform cloud and albedo properties and various levels of absorption within the atmosphere. The evaluation of circular polarisation is challenging; a number of one-photon experiments of  $10^9$  or more is needed to resolve hemispherically-integrated degrees of circular polarisation of a few times  $10^{-5}$ . Last, I introduce brightness curves of Earth obtained with one of the Messenger cameras at three wavelengths (0.48, 0.56 and  $0.63\ \mu\text{m}$ ) during a flyby in 2005. The light curves show distinct structure associated with the varying aspect of the Earth's visible disk (phases of  $98\text{--}107^\circ$ ) as the planet undergoes a full 24h rotation; the structure is reasonably well reproduced with model simulations.

*Keywords:*

---

---

*Email address:* tonhingm@gmail.com (A. García Muñoz)

## 1. Introduction

Our understanding of exoplanetary atmospheres relies on the remote sensing of radiation that, arising from the host star or the planet itself, becomes imprinted with some of the planet's atmospheric features. Ongoing technological developments, to be implemented in >30-m ground-based telescopes and dedicated space missions, are steadily increasing the number of exoplanets amenable to atmospheric characterisation. In the foreseeable future, sophisticated instruments will allow us to separate the radiation of an Earth twin from the glare of its host star (e.g. Traub & Oppenheimer, 2010, and refs. therein). At that moment, it will be possible to address questions such as the occurrence of life on the planet by searching for selected biosignatures in its reflected and/or emitted spectrum (e.g. Brandt & Spiegel, 2014; Des Marais et al., 2002; Seager et al., 2005; Sparks et al., 2009)

In preparation for that moment, modellers have been setting up and testing the tools with which one day the (one pixel, at first) images of Earth-like exoplanets will be rationalized (e.g. Ford et al., 2001; Karalidi et al., 2011, 2012; Karalidi & Stam, 2012; Robinson et al., 2011; Stam, 2008; Tinetti et al., 2006; Zugger et al., 2010, 2011). As some of those works have shown, the information contained in spectra and colour photometry of the one-pixel images will inform us about aspects of the planet such as its atmospheric composition, existence of clouds, and land/ocean partitioning. A key aspect of models, and one that is investigated here, is their capacity to predict an exoplanet's remote appearance and, in particular, how to treat the three-dimensional nature of the atmospheres. The need for such a treatment becomes more apparent as a number of groups are beginning to explore the coupled effects of atmospheric dynamics, heat redistribution and chemistry in the framework of General Circulation Models (e.g. Carone et al., 2014; Joshi, 2003; Kataria et al., 2014; Menou, 2012; Zalucha et al., 2013).

Modelling radiative transport in three-dimensional atmospheres is a computationally intensive task. For that reason it is important to explore all possible avenues. The two most usual approaches to the problem are:

1. The planet disk is partitioned into an  $n_x \times n_y$  number of disk elements. The outgoing radiation is calculated at each discrete element under the approximation of locally plane-parallel atmosphere; then, each discrete contribution is properly added up to generate the disk-integrated magnitude. Its computational cost is proportional to  $n_x \times n_y$ . As an example, simulating a fully-illuminated planet at the  $2^\circ \times 2^\circ$  resolution level involves 8100 separate calculations.
2. Disk integration is directly approached by means of Monte Carlo (MC) integration. The MC scheme conducts one-photon numerical experiments, each of them tracing a photon trajectory through the atmospheric medium. Repeating the experiment  $n_{\text{ph}}$  times results in an estimate of the disk-integrated outgoing radiation that converges to the exact magnitude with a standard deviation that follows a  $\sim n_{\text{ph}}^{-1/2}$  law. Ford et al. (2001) utilised a Forward MC algorithm to investigate the diurnal variability of the Earth's brightness. Forward refers to the tracing of the photons start-

ing from the radiation source onwards through the atmospheric medium, *i.e.* in the same order as the actual photon displacements. In the MC approach, the total computational cost is proportional to  $n_{\text{ph}}$ .

Recent work has introduced an alternative approach based on Pre-conditioned Backward Monte Carlo (PBMC) integration of the vector Radiative Transport Equation (García Muñoz & Mills, 2014). Past applications of the PBMC model to the problem of scattering from a spatially-unresolved planet focused on atmospheres that might be stratified in the vertical but exhibited otherwise uniform optical properties in the horizontal direction. The importance of accounting for three-dimensional effects in the description of the optical properties of exoplanets has been substantiated by a number of works (Ford et al., 2001; Karalidi & Stam, 2012; Karalidi et al., 2012; Tinetti et al., 2006).

Here, I investigate further the PBMC approach and use it to explore Earth's remote appearance for non-uniform distributions of cloud and surface properties. The methodology may find application in the interpretation of earthshine observations (e.g. Arnold et al., 2002; Bazzon et al., 2013; Sterzik et al., 2012; Woolf et al., 2002) and in related research fields such as climate studies that are concerned with planet-averaged properties. This is ongoing work that demonstrates the potentiality of the PBMC approach to become a reference technique in the production of disk-integrated curves for exoplanets.

Section §2 introduces the method, §3 describes the atmospheric, cloud and surface properties implemented in the current exploration exercise, and §4 comments on the phase and diurnal light curves of Earth for a few wavelengths and two different cloud covers. Finally, section §5 introduces the brightness light curves of Earth obtained with images from the 2005 Earth flyby of the Messenger spacecraft, and §6 summarises the main conclusions and touches upon follow-up work.

## 2. The PBMC algorithm

The fundamentals of the PBMC algorithm have been described (García Muñoz & Mills, 2014), and the model has been validated for horizontally-uniform atmospheres (García Muñoz & Mills, 2014; García Muñoz et al., 2014). The validation exercise included a few thousand solutions from the literature for plane-parallel media, disk-integrated model solutions for Rayleigh-scattering atmospheres and measurements of the disk-integrated brightness and polarisation of Venus. In the comparison against other model calculations, typical accuracies of 0.1% and better are achieved.

The algorithm calculates the stellar radiation reflected from the whole disk for planets with stratified atmospheres. The calculation proceeds by simulating a sequence of  $n_{\text{ph}}$  one-photon numerical experiments. Being a backward algorithm, each experiment traces a photon trajectory from the observer through the scattering medium. The contribution to the estimated radiation as measured by the observer is built up by partial contributions every time the photon undergoes a collision. The simulation stops when the photon is either fully absorbed in or escapes from the atmosphere. Pre-conditioning refers to a novel scheme that incorporates the polarisation history of the photon (since its departure from the observer's location) into the sampling of propagation directions. Pre-conditioning prevents spurious behaviours in conservative, optically-thick, strongly-polarising media, and accelerates the convergence over the non-pre-conditioned treatment.

The algorithm includes a scheme to select the photon entry point into the atmosphere based on the local projected area of the 'visible' planet disk (García Muñoz & Mills, 2014). This strategy ensures that all simulated photons contribute to the estimated radiation at the observer's location. In this approach, each solution to the radiative problem is specific to the details of the illuminated disk as viewed by the observer. Changing that view requires a new radiative transport calculation. The implementation is based on the vector Radiative Transport Equation, which entails that the model computes the disk-integrated Stokes vector of the planet. Not explored in past applications of the PBMC approach, the model is well suited for investigating planets with non-uniform distributions of clouds and albedos.

### 3. Atmospheric and surface model

The PBMC algorithm handles elaborate descriptions of the atmospheric, cloud and surface optical properties of the planet. To keep the number of parameters reasonable, however, it is convenient to introduce various simplifications, which are described in what follows.

The model atmosphere adopted here includes gas and clouds and utilises a 30-slab vertical grid with resolutions of 1, 2 and 4 km for altitudes in the 0–10, 10–30 and 30–70 km ranges. The gas is stratified with a scale height of 8 km and the total Rayleigh optical thickness is parameterised by  $\tau_g = 0.1(0.555/\lambda [\mu\text{m}])^4$ . Clouds are placed in a single slab and assumed to be composed of liquid water and have wavelength-dependent real refractive indices ranging from 1.34 at 0.47  $\mu\text{m}$  to 1.30 at 2.13  $\mu\text{m}$ . The considered cloud droplet sizes have an effective radius and variance of  $r_{\text{eff}} = 7.33 \mu\text{m}$  and  $v_{\text{eff}} = 0.12$ , respectively, which is appropriate for continental stratus clouds (Hess et al., 1998). The scattering matrix for the polarisation calculations is determined from Mie theory (Mishchenko et al., 2002). The cloud optical thickness  $\tau_c$  is assumed to be the same for all clouds on the planet. The model atmosphere includes absorption by ozone in the Chappuis band (Jacquinet-Husson et al., 2005). The ozone vertical profile peaks in the stratosphere at 25 km and has an integrated column of 275 Dobson units (Loughman et al., 2004). Ozone absorption is stronger between 0.55 and 0.65  $\mu\text{m}$ , and its effect on the radiative transport calculations is particularly distinct in that spectral range. No other gas molecular bands were considered, and therefore the study focuses on the spectral continuum rather than on strong absorption molecular features. Future work will investigate the potential advantages of introducing the spectral direction into the Monte Carlo integration. Foreseeably, associating each one-photon experiment with a properly-selected wavelength (over an instrument's bandpass) and with a photon entry point into the atmosphere may lead to further computational savings in the simulation of spectra with respect to the usual strategy of stacking many monochromatic calculations and subsequently degrading the so-formed spectrum. The savings are likely to be significant if the final spectra are only required at moderate-to-low resolving powers.

At the planet surface, the model adopts the MODIS white-sky albedos specific to early August 2004 (Moody et al., 2005).<sup>1</sup> The albedos are available at bands centered at 0.47, 0.555, 0.659, 0.858, 1.24, 1.64 and 2.13  $\mu\text{m}$ , which cover much of the spectrum dominated by reflected radiation. The bandwidths of the MODIS filters are of 20–50 nm (Xiong et al., 2009). The monochromatic model calculations presented here are carried out at the MODIS central wavelengths. The prescribed albedos are identically zero over the ocean. Surface reflection is throughout assumed to be of Lambertian type. Specular reflection at the ocean, which may contribute to the planet signal at large phase angles (Robinson et al., 2010; Williams & Gaidos, 2008; Zugger et al., 2010, 2011), will be implemented in later work.

The adopted maps of cloud fraction are from MODIS data<sup>2</sup> specific to 3rd August 2005 (see Section §5). For each one-photon experiment, a scheme based on the local cloud fraction  $f_c$  at the photon entry point into the atmosphere determines the surface albedo to be utilised in that specific photon trajectory simulation and whether the photon is traced through a gas-only or gas-plus-cloud medium. Internally, the scheme draws a random number  $\rho_c \in [0, 1]$ . If  $\rho_c \leq f_c$ , the photon is traced through an atmosphere of optical thickness  $\tau_g + \tau_c$  with optical properties within each slab properly averaged over the gas and cloud. Otherwise, if  $\rho_c > f_c$ , the photon is traced through a gas-only atmosphere of optical thickness  $\tau_g$ .

Both the input surface albedo and cloud fraction maps are averaged and mapped onto longitude/latitude maps of  $2^\circ \times 2^\circ$  resolution. Each map is read into the model at the beginning of the run and kept in memory throughout the simulation of the  $n_{\text{ph}}$  one-photon experiments. Figure (1) shows albedo and cloud fraction maps as sampled by the model in a run specific to the Messenger view of Earth on 18:30UT 3rd August 2005.

<sup>1</sup> Accessible through <http://modis-atmos.gsfc.nasa.gov/ALBEDO/>

<sup>2</sup> Accessible through the MODIS Terra and Aqua Daily Level-3 Data site, [http://gdata1.sci.gsfc.nasa.gov/daac-bin/G3/gui.cgi?instance\\_id=MODIS\\_DAILY\\_L3](http://gdata1.sci.gsfc.nasa.gov/daac-bin/G3/gui.cgi?instance_id=MODIS_DAILY_L3)

## 4. Model results

### 4.1. A look into convergence

In the implementation of the PBMC algorithm, the irradiance  $\mathbf{F}$  at the observer's location is evaluated through a summation:

$$\mathbf{F} = \frac{\pi}{2}(1 + \cos(\alpha)) \frac{1}{n_{\text{ph}}} \sum_{i=1}^{n_{\text{ph}}} \mathbf{I}(u_i, v_i), \quad (1)$$

where  $\mathbf{I}(u_i, v_i)$  is the outgoing radiance Stokes vector from the  $i$ -th one-photon experiment, the uniform random variables  $u, v \in [0, 1]$  sample the planet visible disk and  $\alpha$  is the star-planet-observer phase angle (García Muñoz & Mills, 2014). Equation (1) is effectively an arithmetic average and its convergence properties depend on the dispersion in the outcome of the one-photon experiments.  $F_I$  is the first element of  $\mathbf{F}$  and in the adopted normalisation it is identical to  $A_g \Phi(\alpha)$ , where  $A_g$  is the planet's geometric albedo and  $\Phi(\alpha)$  ( $\Phi(0) \equiv 1$ ) is the planet's scattering phase function. Properly, the planet's scattering phase function also depends on the optical properties of the planet as viewed from the observer's location, and they may change over time.

To investigate the convergence properties of  $\mathbf{F}$ , it is convenient to introduce  $\sigma_I$  that defines the standard deviation for the first element  $I$  of  $\mathbf{I}$  after  $n_{\text{ph}}$  one-photon experiments:

$$\sigma_I^2 = \frac{1}{n_{\text{ph}} - 1} \left( \frac{1}{n_{\text{ph}}} \sum_{i=1}^{n_{\text{ph}}} I_i^2 - \left( \frac{1}{n_{\text{ph}}} \sum_{i=1}^{n_{\text{ph}}} I_i \right)^2 \right), \quad (2)$$

and where  $I_i$  is a short form for  $I(u_i, v_i)$ . In turn, for  $F_I$ :

$$\sigma_{F_I} = \frac{\pi}{2}(1 + \cos(\alpha)) \sigma_I. \quad (3)$$

Analogous expressions can be written for the other elements of  $\mathbf{F}$ :  $F_Q$ ,  $F_U$  and  $F_V$ .

Figure (2) shows histograms of the  $I_i \pi(1 + \cos(\alpha))/2$  values obtained in the application of Eq. (1) to one of the atmospheric configurations discussed in §5. The top panel corresponds to Rayleigh atmospheres at  $0.48 \mu\text{m}$  above a black surface (black curve) or above the non-uniform MODIS albedo map (red curve). A non-uniform surface albedo leads to a slightly broader histogram and a correspondingly larger value of  $\sigma_{F_I}/F_I$ , as shown in Table (1).  $\sigma_{F_I}/F_I$  is indeed a measure of the accuracy associated with the estimated  $F_I$  after  $n_{\text{ph}}$  one-photon experiments.

The bottom panel of Fig. (2) shows the histograms obtained for configurations that in addition incorporate the MODIS cloud map (black and red curves,  $\tau_c=1$  and  $10$  respectively) or a continuous cloud cover of optical thickness  $\tau_c=10$  (green curve). From the comparison of the two panels, it becomes clear that clouds broaden the possible outcome from the single-photon experiments, which affects the accuracy of the algorithm for a prescribed number of one-photon experiments. From the values of  $\sigma_{F_I}/F_I$  and computational times for  $n_{\text{ph}}=10^5$  listed in Table (1), it is straightforward to estimate the accuracy and computational time for an arbitrary  $n_{\text{ph}}$ . In all cases, estimates of  $F_I$  accurate to within 3% (1%) can be obtained in about 1 (10) minutes. A clear advantage of the current approach is that there is little or no overhead associated with the integration over a non-uniform disk, as shown in Table (1).

### 4.2. Earth simulations from $0.47$ to $2.13 \mu\text{m}$

#### 4.2.1. Brightness and degree of linear polarisation

The number of possibilities to explore in terms of viewing geometries and surface/atmosphere configurations is infinite. Important conclusions for configurations that include polarisation have been presented in the literature (e.g. Bailey, 2007; Karalidi et al., 2011, 2012; Karalidi & Stam, 2012; Stam, 2008; Zugger et al., 2010, 2011). To demonstrate the PBMC algorithm, here I will focus on the impact of the cloud optical thickness and adopt  $\tau_c=0$  and  $5$  for two separate sets of calculations. It is assumed that the planet follows an edge-on circular orbit with the sub-observer point permanently on the equator of the planet. Because with the present definition of  $F_Q$  and  $F_U$ , the relation  $|F_U| < |F_Q|$  generally holds (see Section §4.2.1), only  $F_I$  and  $F_Q/F_I$  are considered here.

Figure (3) corresponds to  $\tau_c=0$  (brightness  $F_I$  on the left and polarisation  $F_Q/F_I$  on the right) and shows essentially Rayleigh-scattering phase curves (Buenzli & Schmid, 2009). The cloud-free calculations were carried out with  $n_{\text{ph}}=10^5$ , which entails that the results are accurate to better than 1%. For each wavelength, the different colour curves correspond to different sub-observer longitudes. Local changes in the albedo (and in particular, whether land/ocean dominate the field of view) modulate both the brightness and polarisation of the planet. The modulation is stronger at the longer wavelengths because the Rayleigh optical thickness drops rapidly with wavelength. Figure (4) substantiates the dependence of  $F_I$  and  $F_Q/F_I$  on the sub-observer longitude, or equivalently, on local time.

Figures (5)–(6) are analogous to Figs. (3)–(4) but incorporate the MODIS map of cloud fractions for 3rd August 2005, clouds located at 2–3 km altitude and optical thickness  $\tau_c \sim 5$ . The implemented cloud droplets' scattering cross sections vary by less than 10% from  $0.47$  to  $2.13 \mu\text{m}$ , which justifies the adoption of a wavelength-independent optical thickness for the clouds. The calculations were carried out with  $n_{\text{ph}}=10^6$  to ensure relative accuracies  $\sigma_{F_I}/F_I \sim 3\%$ . In the comparison between the cloud-free and cloud-covered configurations, two basic conclusions emerge. First, the curves for  $\tau_c=5$  show a dependence with phase angle that reveals some basic properties of the scattering cloud particles. Indeed, the polarisation phase curves show a peak at  $\alpha=30\text{--}40^\circ$  due to the primary rainbow of water droplets (Bailey, 2007; Karalidi et al., 2011, 2012; Stam, 2008). Second, clouds attenuate much of the diurnal variability and, typically, the diurnal modulation in brightness is easier to pick up than the modulation in polarisation.

Stam (2008) and follow-up work (Karalidi & Stam, 2012; Karalidi et al., 2011, 2012) have explored the appearance in both brightness and polarisation of Earth-like exoplanets. Stam (2008) and Karalidi et al. (2011) introduce the concept of quasi-horizontally inhomogeneous planets, which allows them to estimate the outgoing radiation from a horizontally non-uniform planet as a weighted sum of the signal from uniform-planet solutions. Their weighting scheme is based on the fractional coverage of each uniform configuration. Karalidi & Stam (2012) and Karalidi et al. (2012), however, utilise a fully inhomogeneous treatment of the planet.

Comparison of Fig. 13 of Stam (2008) at wavelengths of 0.44 and 0.87  $\mu\text{m}$  and Fig. (4) here at wavelengths of 0.47 and 0.858  $\mu\text{m}$  is relevant. For cloud-free conditions and a phase angle  $\alpha=90^\circ$ ,  $F_I \sim 0.03\text{--}0.04$  and  $F_Q/F_I \sim 0.8$  at the shorter wavelength in both works. At the longer wavelength, also for  $\alpha=90^\circ$ , Stam (2008) reports three distinct peaks at different sub-observer longitudes and highest  $F_I$  values of 0.06. The three-peak structure is reproduced by the calculations presented here, but the highest  $F_I$  here is 0.045, somewhat lower than 0.06 in Stam (2008). The different treatment of the albedo in the two works, in particular their magnitudes and the absence of Fresnel reflection in the current one, is a likely reason for the discrepancy. In polarisation, both works show clear structure that correlates inversely with the brightness. The intensity of the  $F_Q/F_I$  peaks, however, differs between the two works. Since high  $F_Q/F_I$  values typically match dark areas of the planet, again, the discrepancies between the two works probably arise from the different treatment of the surface albedo.

Similarly, comparison of Fig. 14 of Stam (2008) and Fig. (6) here reveals information about the role of clouds. It is difficult to draw definite conclusions from the comparison between the two sets of curves because the optical thickness and droplet size of the clouds implemented in each work are different. The two sets show, however, that the diurnal variability of both  $F_I$  and  $F_Q/F_I$  is highly attenuated at the shorter wavelength, but that the variability in  $F_I$  is still distinct at the longer one.

Karalidi & Stam (2012) and Karalidi et al. (2012) investigate further the simulated signal from Earth-like exoplanets and take into account non-uniform cloud and albedo properties. Karalidi et al. (2012) consider a realistic cloud map based on MODIS data. Their work emphasises the detectability of features like the primary rainbow, which originates from Mie scattering in spherical droplets but may be masked by scattering in ice particles; and, the impact of non-uniformities on the disk-integrated signal. A case-by-case comparison between those works and the results presented in Figs. (3)–(6) here is not feasible. It is worth noting, nevertheless, that the main features that appear in the curves of Figs. (5)–(6) here are also found in Figs. 6–8 of Karalidi et al. (2012). This includes the occurrence of the primary rainbow in both  $F_I$  and  $F_Q/F_I$ . The significant variety in the curves reported in those works and here illustrates the complexity of the problem. It also cautions against quick conclusions when the time comes that either brightness or polarisation curves of Earth-like exoplanets become available.

The near infrared (e.g. 1.55–1.75; 2.1–2.3  $\mu\text{m}$ ) has been proposed as a better option than visible wavelengths in the characterisation of surface features that might occur at specific local times (high/low reflecting surfaces such as desert/ocean, respectively) and phase angles (specular reflection from an ocean) (Zugger et al., 2011). The simulations here (see curves for  $\lambda > 1 \mu\text{m}$  in Figs. 3 and 5) confirm (compare to Fig. 3 in Zugger et al. (2011)) that contrasts in the near infrared can be high for cloud-free conditions, but become less distinct at moderate cloud opacities. Since the current implementation of the PBMC model does only account for Lambert reflection at the surface, a more direct comparison with Zugger et al. (2011) is not immediately possible.

#### 4.2.2. Angle of linear polarisation

Non-uniform surface albedos and patchy clouds introduce an asymmetry between the northern and southern hemispheres that may lead to non-zero values of  $F_U$ . The angle of polarisation  $\chi$ , defined through  $\tan 2\chi = F_U/F_Q$ , expresses the orientation of the outgoing polarisation vector with respect to the reference plane. The reference plane is normal to the planet scattering plane; the latter is formed by the viewing and illumination directions. Because each photon is tracked with respect to the same three-dimensional absolute rest frame and the same reference plane is utilised to express the Stokes vector, all the photons' Stokes vectors can be added without further manipulation. The model calculations presented above show, however, that the hemispherically-averaged  $U$  components take different signs at the northern and southern hemispheres and that summation over the entire disk leads to the effective cancellation of  $F_U$ , i.e.  $|F_U/F_Q| \ll 1$  away from the neutral points where  $F_Q \approx 0$ .

For reference, Fig. (7; solid curve) shows the change in the ratio  $F_U/F_Q$  with phase angle at a wavelength of 0.555  $\mu\text{m}$  and sub-observer longitude of  $0^\circ$  in one of the cloud-covered configurations investigated in Fig. (5). The ratio  $F_U/F_Q$  remains small at all phase angles, with deviations to that trend arising where  $F_Q$  becomes small and the statistical errors large. Thus, the planet's polarisation vector is preferentially aligned with the planet scattering plane (if  $F_Q < 0$ ) or with the reference plane (if  $F_Q > 0$ ), also in the presence of non-uniformities at both the surface and cloud levels.

It is possible to assess what occurs within a molecular absorption band by setting the single scattering albedo in the atmospheric model  $\varpi < 1$ . The dashed curve in Fig. (7) presents the ratio  $F_U/F_Q$  for an adopted  $\varpi = 0.1$  at all altitudes. In those conditions, single scattering dominates and the ratio  $F_U/F_Q$  becomes smaller. According to the calculations shown in Fig. (7), the angle of linear polarisation  $\chi$  is either close to zero or to  $\pi/2$  both within and outside molecular absorption bands.

#### 4.2.3. Circular polarisation

Circular polarisation in the light scattered from planetary atmospheres typically results from two or more collisions of the photons within the medium. In the cases that measurements have been attempted (e.g. Kemp et al., 1971; Sparks et al., 2005; Swedlund et al., 1972), the degree of circular polarisation is orders of magnitude smaller than for linear polarisation, which entails that observations of circular polarisation are always challenging.

Unlike abiotic material, living organisms may lead to distinct circular polarisation signatures (e.g. Sparks et al., 2009) potentially amenable to remote sensing. Indeed, the prospects of using circular polarisation as a biomarker in the investigation of habitable exoplanets has prompted new research on this front (e.g. Nagdimunov et al., 2014; Sparks et al., 2009).

The Earth model considered here does not include circular polarisation effects associated with living organisms. It is relevant, nevertheless, to assess the suitability of the PBMC algorithm for a prospective investigation of biogenic circular polarisation. On the basis of the configurations investigated in Fig. (5) for cloudy atmospheres, I have calculated  $F_V/F_I$  vs. phase

angle at the wavelengths of 0.470, 0.555 and 0.659  $\mu\text{m}$  and a sub-observer longitude of  $0^\circ$ . The calculations are presented in Fig. (8) separately for the northern and southern hemispheres, and with  $n_{\text{ph}}=10^9$  and  $10^{10}$  one-photon experiments per phase angle. As expected (Kawata, 1978; Kemp et al., 1971), the two hemispheric components have comparable magnitudes but opposite signs, and tend to cancel out when the integration is extended over the entire planet disk. The numerical experiments suggest that a number  $n_{\text{ph}}=10^9$  of one-photon numerical experiments are needed to reach acceptable accuracies. This is about three orders of magnitude more than the needs for linear polarisation, which conveys one of the difficulties in predicting and interpreting circular polarisation features.

## 5. Messenger diurnal light curves

On cruise towards Mercury, the NASA Messenger spacecraft performed an Earth flyby in August 2005 (McNutt et al., 2008). Observations of Earth during the gravity assist include imagery with the Mercury Dual Imaging System (MDIS) cameras. Of particular interest here are the colour sequences of full-disk images captured with the Wide Angle Camera (WAC) on the departure leg. Each sequence comprises nearly-simultaneous observations over a narrow-band filter of band center/width ( $\mu\text{m}$ ),  $\lambda/\Delta\lambda = 0.480/0.01$ ,  $0.560/0.006$  and  $0.63/0.0055$ . With a cadence of 3 images every 4 minutes, the total number of images amounts to 1080.

As the spacecraft departs, the Earth angular diameter evolves from  $10.2^\circ$  (nearly filling the WAC field of view of  $10.5^\circ$ ) at the start of the sequence to  $1.6^\circ$  at the end of the sequence 24 hours later. At its farthest during the sequence (about 457,000 km from Earth), the spacecraft is beyond the Moon orbit. Correspondingly, the Sun-planet centre-spacecraft phase angle  $\alpha$  varies from  $107^\circ$  to  $98^\circ$ . Figure (9) presents the two geometric parameters against time since the start of the sequence on 2nd August at about 22:31UT.

The WAC images were downloaded from the Planetary Data System and read with the software made available at the Small Bodies Node.<sup>3</sup> The basic treatment of the images is similar to that outlined by Domingue et al. (2010) in their analysis of the whole-disk optical properties of Mercury. Integration of the planet brightness was conducted over a rectangular box that contains the Earth visible disk. Residual background values were estimated from two stripes running north-south on each side of the box. When possible, the box was designed to extend beyond the visible edge by 0.2–0.3 Earth radii, and the adjacent stripes were 10 pixel wide. Other combinations of box size and stripe width resulted in very similar conclusions. The corrected brightness was then summed over the integration box and multiplied by the solid angle per pixel to yield the planet's irradiance as measured from the spacecraft vantage point,  $F_p$ . To derive the planet phase function  $A_g\Phi$ , I applied the equation:

$$F_p = \left(\frac{R_p}{\Delta}\right)^2 \left(\frac{1}{a_\star[\text{AU}]}\right)^2 A_g\Phi F_\star, \quad (4)$$

where  $R_p$  is the Earth's mean radius ( $=6371$  km),  $\Delta$  is the spacecraft-to-Earth centre distance, and  $a_\star$  is the Earth's orbital distance.  $F_\star$  is the solar irradiance at 1 Astronomical Unit specific to the camera filter (Mick et al., 2012). A related magnitude, the apparent albedo, can be obtained from:

$$A_{\text{app}} = \frac{A_g\Phi(\alpha)}{(A_g\Phi(\alpha))_{\text{Lambert}}} = \frac{A_g\Phi(\alpha)}{\frac{2}{3}\frac{1}{\pi}[\sin\alpha + (\pi - \alpha)\cos\alpha]}, \quad (5)$$

that refers  $A_g\Phi(\alpha)$  to that for a Lambert sphere.

Figure (10) shows the Messenger  $A_g\Phi$  light curves (top panel; solid) against time for each colour filter. For comparison, Mallama (2009) reports  $A_g\Phi(90^\circ)=0.06$  and  $A_g\Phi(120^\circ)=0.05$  from earthshine observations in broadband

visible light (Goode et al., 2001). The Messenger curves exhibit variations of peak-to-peak amplitude up to  $\sim 20\%$  over times of hours, which is consistent with the findings by EPOXI (Livengood et al., 2011).

The evolving phase angle precludes an interpretation of the light curves based solely on diurnal changes in the Earth cover. A detailed observation-model analysis is deferred to future work. It is worth noting, however, that the model captures the major features in the Messenger light curves. Using the atmosphere/surface prescriptions of §3 (and in particular, the albedo maps at  $0.47$ ,  $0.555$  and  $0.658 \mu\text{m}$ , the latter being somewhat off-set from the MDIS/WAC band centre), the Messenger  $A_g\Phi$  points are reasonably well reproduced by the model calculations (Fig. 10; top panel; dashed) that incorporate the MODIS cloud map specific to 3rd August 2005, clouds located at 2–3 km altitude and optical thickness  $\tau_c \sim 3$ , and the relevant viewing/illumination geometry. The space of model parameters is vast and other atmospheric configurations can plausibly lead to similar or better fits. At the relevant phase angles, the model predicts strong polarisation at all three wavelengths, as shown in Fig. (10; middle panel). The model calculations were made with  $n_{\text{ph}}=10^7$ , which entails standard deviations  $\sigma_{F_I}/F_I \sim \sigma_{F_Q}/F_Q \sim 1\%$ . The bottom panel of Fig. (10) shows the corresponding cloud fraction and surface albedos averaged over the Earth visible disk at each instant during the observing sequence. The drop in cloudiness and increase in surface albedo that occurs half way through the observing sequence, especially at the longer wavelengths, reveals the presence of Africa's vast desert expanses.

In preparation of a more thorough exploration, Fig. (11) investigates the sensitivity of the model-predicted Messenger light curves to the surface albedo. Postulated changes in the reflective properties of the surface are particularly clear from 12 to 20 hours in the observing sequence. This is related to two different factors, namely the low cloud fraction and high surface albedos at the time. Decreased Rayleigh scattering allows photons to penetrate deeper, which leads to increased relative contrasts at the longer wavelength. The simulation above a black surface clearly demonstrates that most, but not all, of the variability in the light curve at the three wavelengths originates from cloud patchiness.

<sup>3</sup> [http://pdssbn.astro.umd.edu/tools/tools\\_readPDS.shtml](http://pdssbn.astro.umd.edu/tools/tools_readPDS.shtml)



## 6. Summary and outlook

Models will play key roles in the interpretation of future observations of exoplanetary atmospheres. Here, I presented a method to predict the disk-integrated Stokes vector of stellar radiation reflected from a planet. The method is flexible and handles variations in the planet optical properties in both the vertical and horizontal directions. A major advantage of this approach is that its computational cost is not significantly affected by non-uniformities at the atmospheric and cloud levels. Being based on Monte Carlo integration, the accuracy (and in turn, the computational time) of a calculation can be established a priori. Typically, solutions for a specific viewing/illumination geometry accurate to within 3% are produced in one minute or less for planet configurations as elaborate as those described here for an Earth replica. In the future, it will be interesting to address a detailed analysis of the Messenger light curves and investigate the complementarity of brightness and polarisation measurements in the characterisation of Earth-like exoplanets over long time baselines.

## Acknowledgments

I gratefully acknowledge the assistance of Jake Ritchie (University of Maryland, MD) with the software for reading the Messenger/MDIS images, and access to the GeoViz software (Henry Throop, <http://soc.boulder.swri.edu/nhgv/>) for the visualization of Earth from the Messenger trajectory. The Messenger/MDIS images were downloaded from the Planetary Data System. I gratefully acknowledge conversations with Tom Enstone (ESA/ESTEC, Netherlands) about the Earth simulations. Finally, I thank Frank P. Mills (Australian National University, Australia) for comments on an early version of the manuscript.

## References

- Arnold, L., Gillet, S., Lardi re, O., Riaud, P., Schneider, J., 2002, A test for the search for life on extrasolar planets. Looking for the terrestrial vegetation signature in the Earthshine spectrum. *Astron. & Astrophys.*, 392, 231–237.
- Bailey, J., 2007, Rainbows, polarization, and the search for habitable planets. *Astrobiology*, 7, 320–332.
- Bazzon, A., Schmid, H.M., Gisler, D., 2013, Measurement of the earthshine polarization in the B, V, R, and I bands as function of phase. *Astron. & Astrophys.*, 556, A117
- Brandt, T.D. & Spiegel, D.S., 2014, arXiv:1404.5337v1
- Buenzli, E., Schmid, H.M., 2009, A grid of polarization models for Rayleigh scattering planetary atmospheres. *Astron. & Astrophys.*, 504, 259–276.
- Carone, L., Keppens, R., Decin, L., 2014, Connecting the dots: A versatile terrestrial planet benchmark for the atmospheres of tidally locked Super-Earths. eprint arXiv:1405.6109.
- Des Marais, D.J., Harwit, M.O., Jucks, K.W., Kasting, J.F., Lin, D.N.C., et al., 2002, Remote Sensing of Planetary Properties and Biosignatures on Extrasolar Terrestrial Planets. *Astrobiology*, 2, 153–181.
- Domingue, D.L., Vilas, F., Holsclaw, G.M., Warell, J., Izenberg, N.R. et al., 2010, Whole-disk spectrophotometric properties of Mercury: Synthesis of MESSENGER and ground-based observations. *Icarus* 209, 101–124.
- Ford, E.B., Seager, S., Turner, E.L., 2001, Characterization of extrasolar terrestrial planets from diurnal photometric variability. *Nature*, 412, 885–887.
- Garc a Mu oz, A., Mills, F.P., 2014, *Astron. & Astrophys.*, *under review*.
- Garc a Mu oz, A., P erez-Hoyos, S., S anchez-Lavega, A., 2014, *Astron. & Astrophys. Lett.*, *accepted for publication*.
- Goode, P.R., Qiu, J., Yurchyshyn, V., Hickey, J., Chu, M.-C., et al., 2001, Earthshine observations of the Earth’s reflectance. *Geophys. Res. Lett.* 28, 1671–1674.
- Hess, M., Koepke, P., Schult, I., 1998, Optical properties of aerosols and clouds: The software package OPAC. *Bull. American Met. Soc.*, 79, 831–844.
- Jacquinet-Husson, N., Scott, N.A., Ch  din, A., Garceran, K., Armante, R., et al., 2005, The 2003 edition of the GEISA/IASI spectroscopic database. *JQSRT*, 95, 429–467.
- Joshi, M., 2003, Climate Model Studies of Synchronously Rotating Planets. *Astrobiology*, 3, 415–427.
- Karalidi, T., Stam, D. M., Hovenier, J.W., 2011, Flux and polarisation spectra of water clouds on exoplanets. *Astron. & Astrophys.*, 530, A69.
- Karalidi, T., Stam, D. M., Hovenier, J.W., 2012, Looking for the rainbow on exoplanets covered by liquid and icy water worlds. *Astron. & Astrophys.*, 548, A90.
- Karalidi, T., Stam, D. M., 2012, Modeled flux and polarization signals of horizontally inhomogeneous exoplanets applied to Earth-like planets. *Astron. & Astrophys.*, 546, A56
- Kataria, T., Showman, A.P., Fortney, J.J., Marley, M.S., Freedman, R.S., 2014, The atmospheric circulation of the super Earth GJ 1214b: Dependence on composition and metallicity. *Astrophys. J.*, 785, id. 92.
- Kawata, Y., 1978, *Icarus*, 33, 217–232.
- Kemp, J.C., Wolstencroft, R.A., Swedlund, J.B., 1971, *Nature*, 232, 165–168.
- Livengood, T.A., Deming, L.D., A’Hearn, M.F., Charbonneau, D., Hewagama, T., et al., 2011, Properties of an Earth-like planet orbiting a Sun-like star: Earth observed by the EPOXI mission. *Astrobiology*, 11, 907–930.
- Loughman, R.P., Griffioen, E., Oikarinen, L., Postlyakov, O.V., Rozanov, A., et al., 2004, Comparison of radiative transfer models for limb-viewing scattered sunlight measurements. *J. Geophys. Res.: Atmospheres*, 109, CiteID D06303.
- Mallama, A., 2009, Characterization of terrestrial exoplanets based on the phase curves and albedos of Mercury, Venus and Mars. *Icarus* 204, 11–14.
- Menou, K., 2012, Atmospheric circulation and composition of GJ1214b. *Astrophys. J. Lett.*, 744, id. L16.
- Mick, A., Murchie, S., Prockter, L., Rivkin, A., Guinness, E., Ward, J., 2012, MESSENGER MDIS CDR/RDR software interface specification. Version 1.2.11.
- McNutt Jr., R.L., Solomon, S.C., Grant, D.G., Finnegan, E.J., Bedini, P.D., the MESSENGER Team, 2008, The MESSENGER mission to Mercury: Status after the Venus flybys. *Acta Astronautica* 63, 68–73.
- Mishchenko, M.I., Travis, L.D., Lacis, A.A., 2002, Scattering, absorption and emission of light by small particles. Cambridge University Press, Cambridge.
- Moody, E.G., King, M.D., Platnick, S., Schaaf, C.B., Gao, F., 2005, Spatially complete global spectral surface albedos: Value-added datasets derived from Terra MODIS land products. *IEEE Transactions on Geoscience and Remote Sensing*, 43, 144–158.
- Nagdimunov, L., Kolokolova, L., Mackowski, D., 2014, Characterization and remote sensing of biological particles using circular polarization. *JQSRT*, 131, 59–65.
- Robinson, T.D., Meadows, V.S., Crisp, David, 2010, Detecting oceans on extrasolar planets using the glint Effect. *Astrophys. J. Lett.*, 721, L67–L71.
- Robinson, T.D., Meadows, V.S., Crisp, D., Deming, D., A’Hearn, M.F., et al., 2011, Earth as an Extrasolar Planet: Earth Model Validation Using EPOXI Earth Observations. *Astrobiology*, 11, 393–408.
- Seager, S., Turner, E.L., Schafer, J., Ford, E.B., 2005, A Possible Spectroscopic Biosignature of Extraterrestrial Plants. *Astrobiology*, 5, 372–390.
- Sparks, W.B., Hough, J.H., Bergeron, L.E., 2005, A search for chiral signatures on Mars. *Astrobiology*, 5, 737–748.
- Sparks, W.B., Hough, J., Germer, T.A., Chen, F., Dassarma, S., et al., 2009, Detection of circular polarization in light scattered from photosynthetic microbes. *Proceedings of the National Academy of Sciences*, 106, 7816–7821.
- Stam, D.M., 2008, Spectropolarimetric signatures of Earth-like extrasolar planets. *Astron. & Astrophys.*, 482, 989–1007.
- Sterzik, M.F., Bagnulo, S., Pall  , E., 2012, Biosignatures as revealed by spectropolarimetry of Earthshine. *Nature*, 483, 64–66.
- Swedlund, J.B., Kemp, J.C., Wolstencroft, R.D., 1972, Circular polarization of Saturn. *Astrophys. Journal*, 178, 257–265.
- Tinetti, G., Meadows, V.S., Crisp, D., Fong, W., Fishbein, E., et al., 2006, Detectability of Planetary Characteristics in Disk-Averaged Spectra. I: The Earth Model. *Astrobiology*, 6, 34–47.

Traub, W.A. & Oppenheimer, B.R., 2010, Direct imaging techniques. In Exoplanets, Ed. S. Seager, (University of Arizona Press, Tucson, Arizona), 111–119.

Williams, D.M., Gaidos, E., 2008, Detecting the glint of starlight on the oceans of distant planets. *Icarus*, 195, 927–937.

Woolf, N.J., Smith, P.S., Traub, W.A., Jucks, K.W., 2002, The spectrum of earthshine: A pale blue Dot observed from the ground. *Astrophys. J.*, 574, 430–433.

Xiong, X., Chiang, K., Sun, J., Barnes, W.L., Guenther, B., Salomonson, V.V., 2009, NASA EOS Terra and Aqua MODIS on-orbit performance. *Adv. Space Res.*, 43, 413–422.

Zalucha, A.M., Michaels, T.I., Madhusudhan, N., 2013, An investigation of a super-Earth exoplanet with a greenhouse-gas atmosphere using a general circulation model. *Icarus*, 226, 1743–1761.

Zugger, M.E., Kasting, J.F., Williams, D.M., Kane, T.J., Philbrick, C.R., 2010, Light Scattering from Exoplanet Oceans and Atmospheres. *Astrophys. J.*, 723, 1168–1179.

Zugger, M.E., Kasting, J.F., Williams, D.M., Kane, T.J., Philbrick, C.R., 2011, Searching for water Earths in the near-infrared. *Astrophys. J.*, 739:12.

Table 1: Summary of performances of the algorithm for disk integration at  $0.48\ \mu\text{m}$  and various Earth configurations discussed in §4.1. Computational times are based on a 2.8 GHz workstation and  $n_{\text{ph}}=10^5$ .

Surf. albedo	Cloud	$\sigma_{F_I}/F_I \times 100$	Comp. time [s]
0	No	0.24	1.5
MODIS	No	0.33	1.4
MODIS	Patchy, $\tau_c=1$	7.8	2.2
MODIS	Patchy, $\tau_c=10$	9.1	7.7
MODIS	Continuous, $\tau_c=10$	7.7	10.4

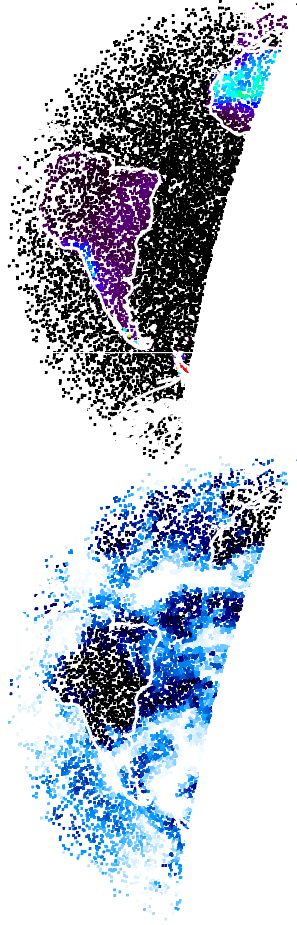


Figure 1: Top. In the PBMC algorithm, each one-photon experiment is associated with a local albedo value. This image shows the surface albedo at  $0.47 \mu\text{m}$  as sampled in a  $n_{\text{ph}}=10^4$  calculation for viewing and illumination conditions specific to the Messenger view of Earth on 18:30UT 3rd August 2005. The phase angle for this view of the Earth is equal to  $98.7^\circ$ . The density of sampling points is based on the projected area of the planet's visible disk, which explains why the sampling points tend to concentrate near the terminator. Bottom. Same as above but showing the cloud fraction  $f_c$ . White and black stand for  $f_c=1$  and  $=0$  respectively.

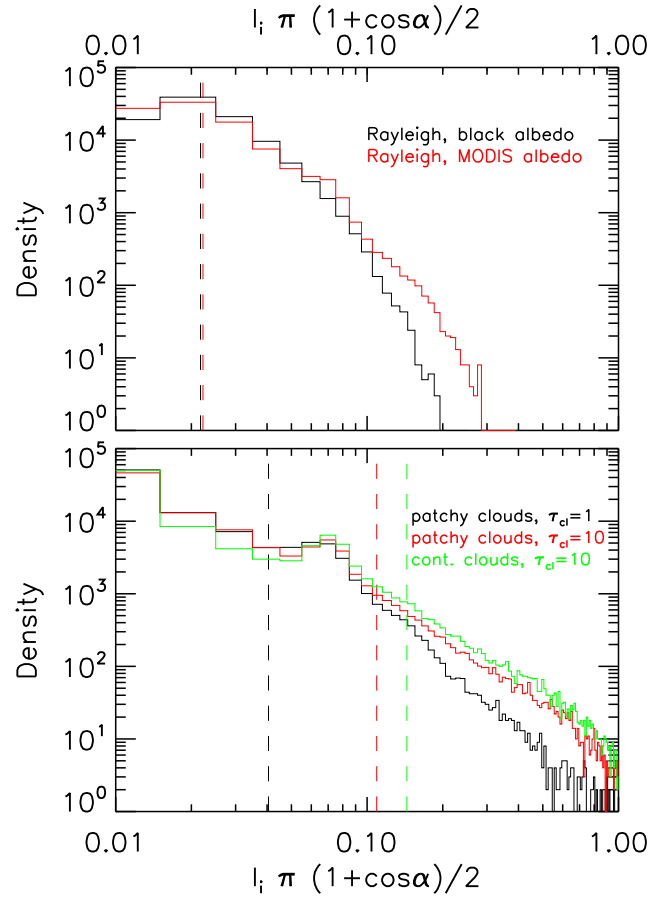


Figure 2: Histograms for the partial evaluations of Eq. (1) with the PBMC algorithm and various surface/cloud configurations. Each experiment comprises a total of  $n_{ph}=10^5$  one-photon realisations. The top and bottom panels are specific to cloud-free and cloud-covered atmospheres respectively. The experiment corresponds to the viewing/illumination geometry of Fig. 1, with  $\alpha=98.7^\circ$ . The dashed vertical lines are mean value estimates for  $F_I$ , as follows from Eq. (1).

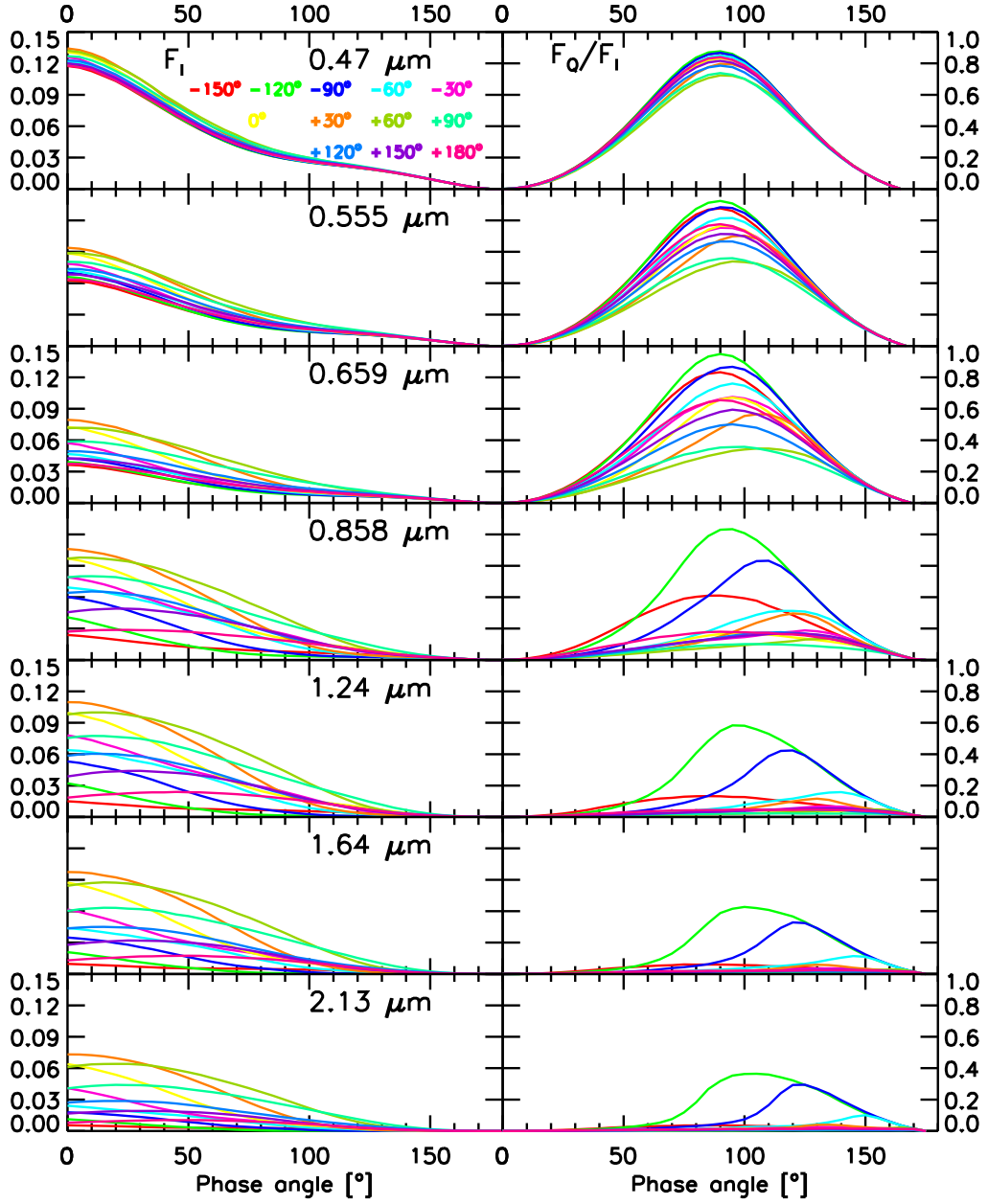


Figure 3: Brightness (left) and polarisation (right) curves for cloud-free conditions. Only the  $\alpha=0-180^\circ$  range is presented. From top to bottom, wavelengths from 0.47 to 2.13  $\mu\text{m}$ . Within each panel, the different colour curves refer to different sub-observer longitudes.

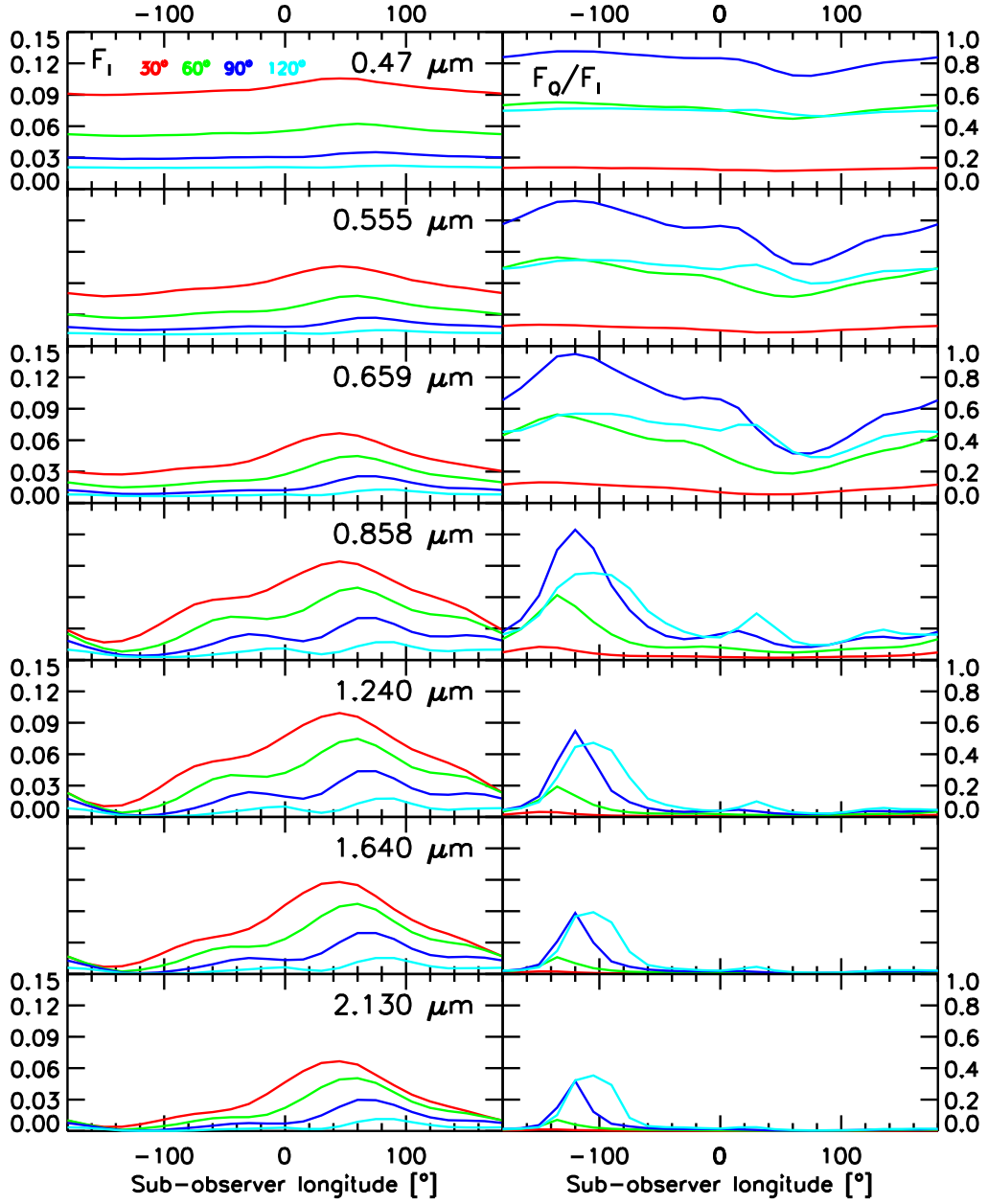


Figure 4: Brightness (left) and polarisation (right) curves for cloud-free conditions. **Equivalent** to Fig. (5) but substantiating modulations with sub-observer longitude or, equivalently, with local time. Within each panel, the different colour curves refer to different phase angles.

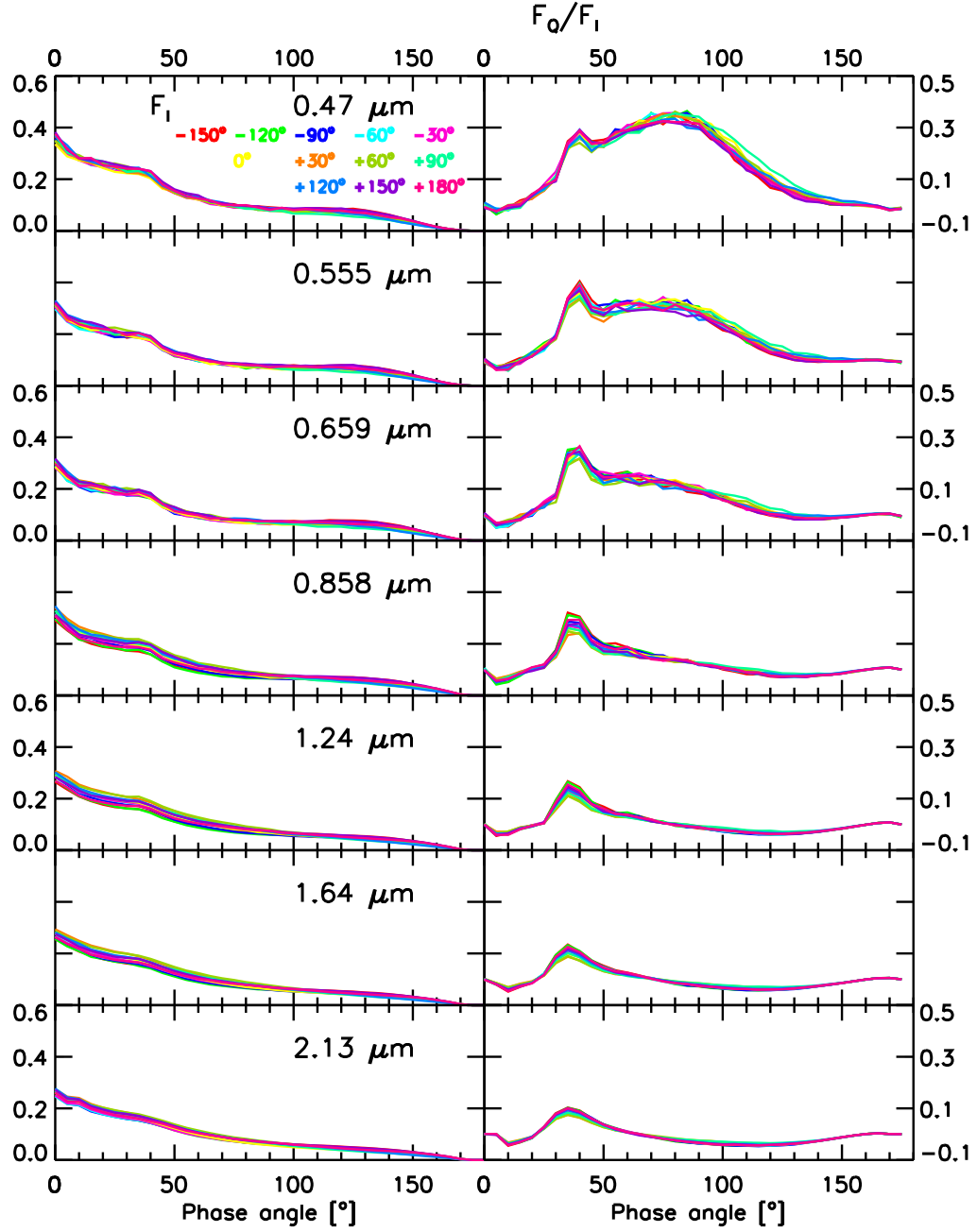


Figure 5: Equivalent to Fig. (3) but for an atmosphere partially covered by clouds of optical thickness  $\tau_c=5$ . The estimated relative accuracy is 3% and 6% for brightness and polarisation.

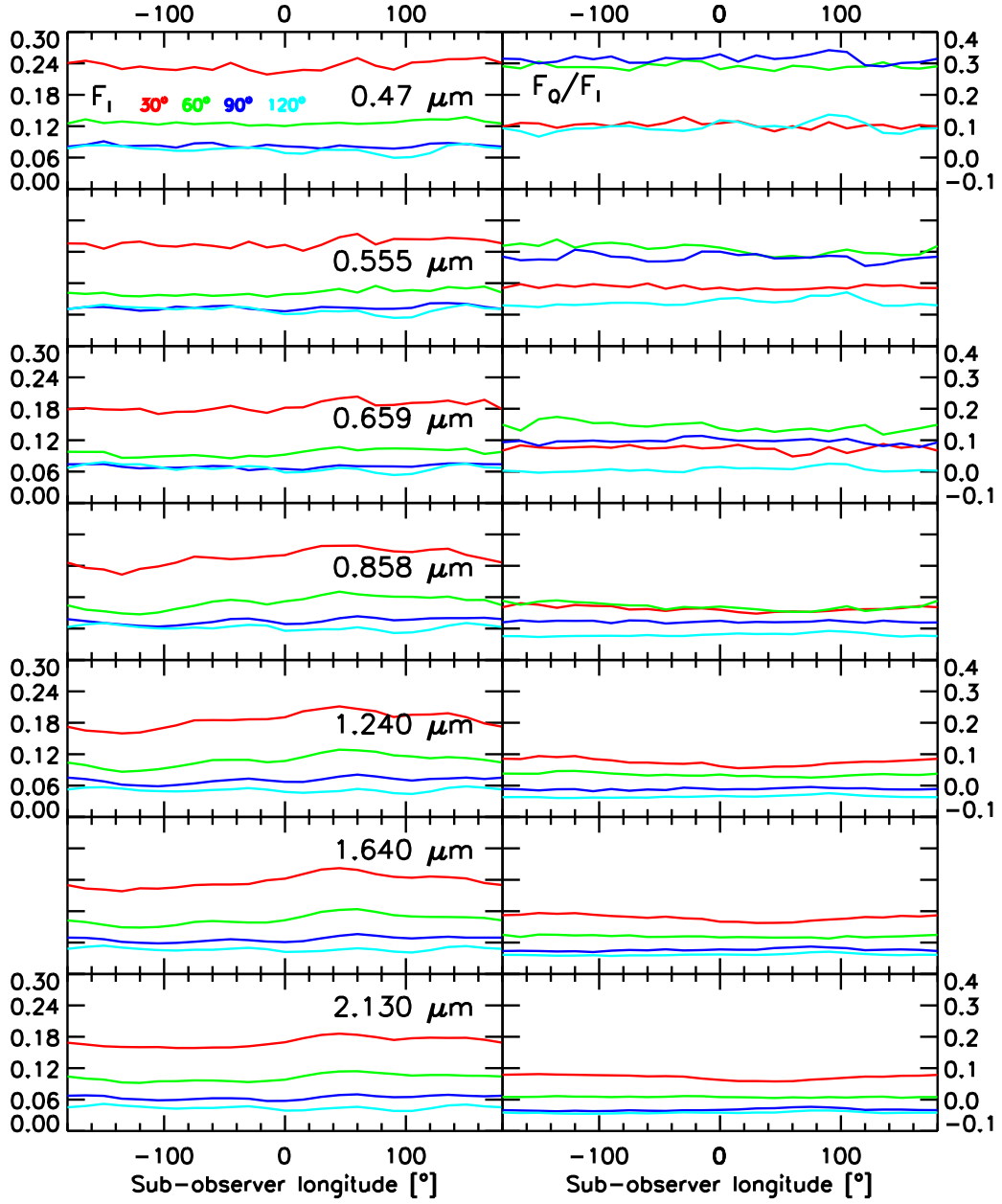


Figure 6: Equivalent to Fig. (4) but for an atmosphere partially covered by clouds of optical thickness  $\tau_c=5$ . The estimated relative accuracy is 3% and 6% for brightness and polarisation.



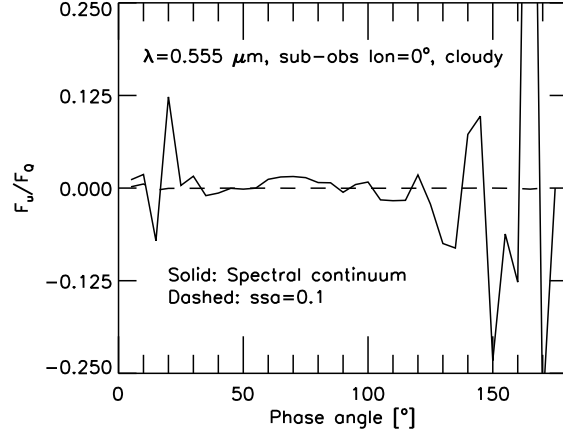


Figure 7: Solid curve: Ratio  $F_U/F_Q$  versus phase angle for the cloudy configuration described in Fig. (5) at a wavelength of  $0.555 \mu\text{m}$  and a sub-observer longitude of  $0^\circ$ . The ratio remains close to zero for most phase angles; deviations to that trend are largely due to  $F_Q$  values nearing zero. Dashed curve: Ratio  $F_U/F_Q$  in the same configuration but with a prescribed atmospheric single scattering albedo ( $\text{ssa} \equiv \sigma$ ) of 0.1 at all altitudes. By minimising the significance of multiple scattering, the dashed curve provides a better insight into conditions within a strong molecular absorption band.

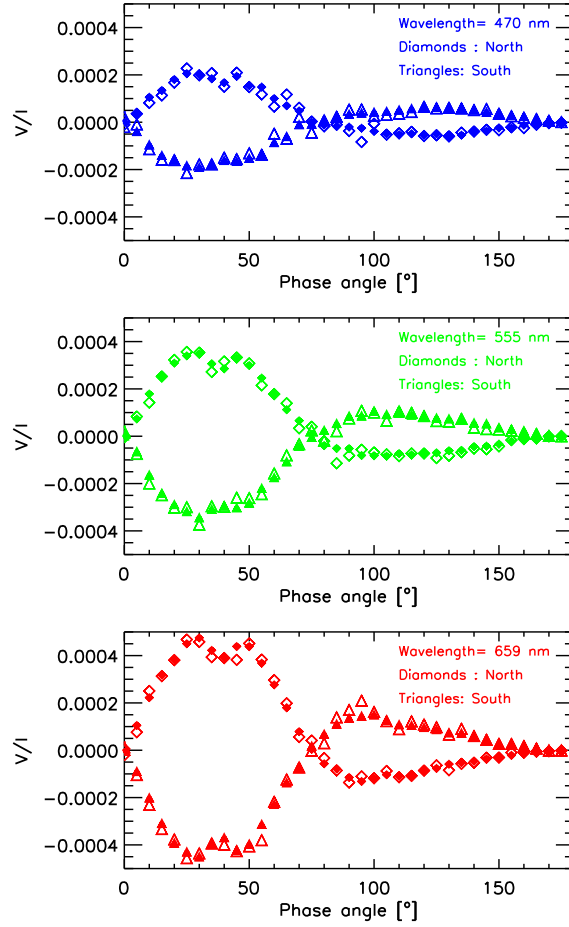


Figure 8: Degree of circular polarisation  $V/I$  for the cloudy configuration described in Fig. (5) at the three specified wavelengths and a sub-observer longitude of  $0^\circ$ . Separate curves are shown for calculations over the northern and southern hemispheres. Open and filled symbols correspond to calculations with  $n_{\text{ph}}$  of about  $10^9$  and  $10^{10}$ , respectively.

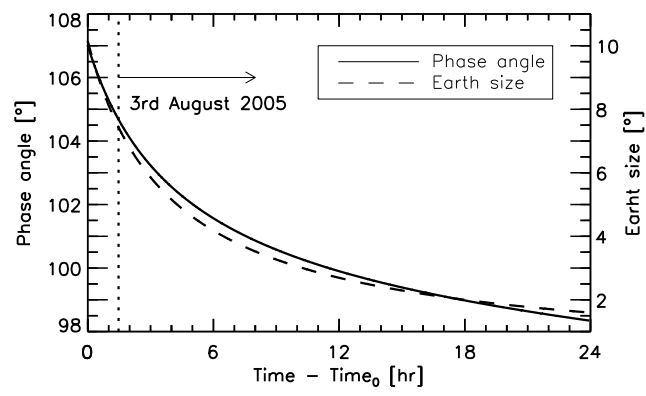


Figure 9: Sun-Earth centre-spacecraft phase angle and apparent angular size of Earth during the Messenger flyby.

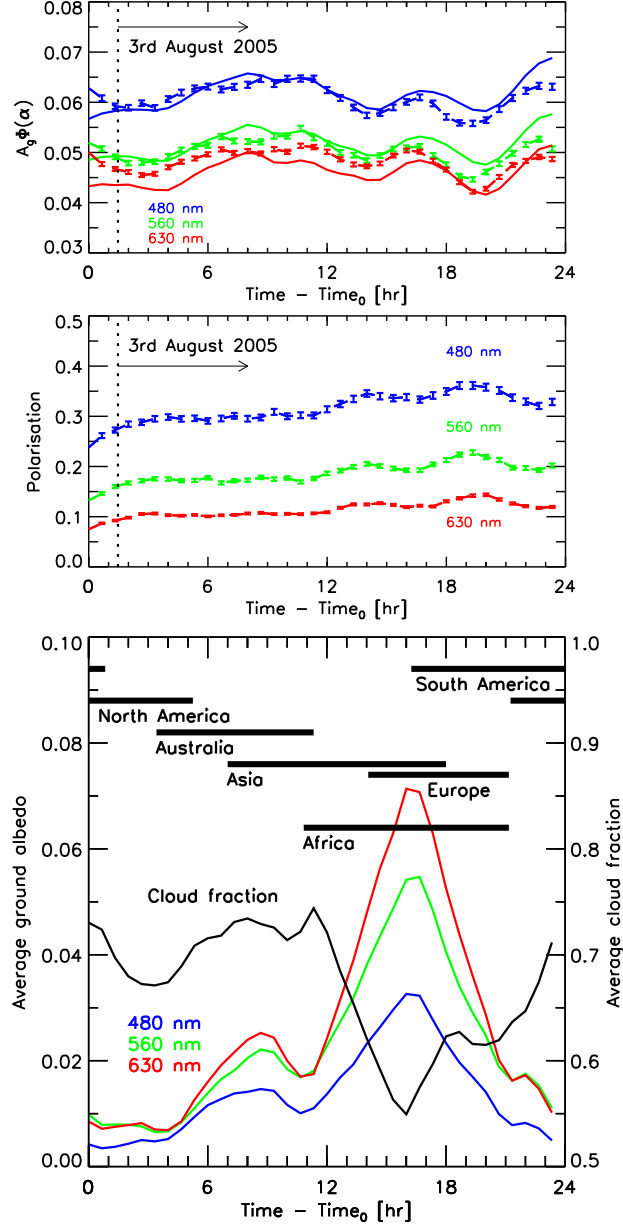


Figure 10: Top panel: Messenger diurnal light curves. Solid curves are Messenger data; dashed curves are model predictions with clouds at 2–3 km altitude and cloud optical thickness  $\tau_c=3$ . For the model predictions, the error bars are standard deviations  $\sigma_{F_I}/F_I \sim 1\%$ . Middle panel: Model-predicted polarisation light curves for the configuration of the top panel. Bottom panel: Average cloud fraction and surface albedos over the Earth visible disk at each instant during the observing sequence.

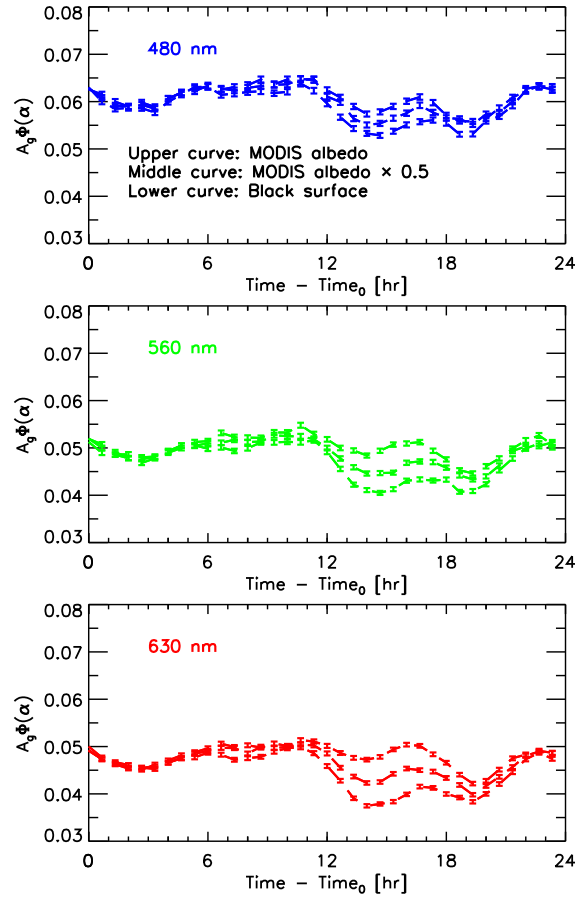


Figure 11: Model-predicted brightness light curves for conditions specific to the Messenger observing sequence. The three curves in each panel represent three differently scaled versions of the surface albedo. The surface becomes more apparent between 12 and 20 hours, with Africa well into the field of view, because the cloud fraction is lower and the surface albedo is higher. The contrast is higher at 630 nm than at either 480 or 560 nm because Rayleigh scattering becomes less efficient at longer wavelengths and more photons penetrate deeper into the atmosphere.